Journal of the European Ceramic Society xxx (xxxx) xxx–xxx

Contents lists available at ScienceDirect

Journal of the European Ceramic Society

journal homepage: www.elsevier.com/locate/jeurceramsoc

Original Article

Microstructure and phase stability of suspension high velocity oxy-fuel sprayed yttria stabilised zirconia coatings from aqueous and ethanol based suspensions

M. Bai, H. Maher, Z. Pala, T. Hussain*

Faculty of Engineering, University of Nottingham, NG7 2RD, UK

ARTICLE INFO

Keywords:
Suspension high velocity oxy fuel (SHVOF)
Yttria-stabilised zirconia (YSZ)
Suspension medium
Microstructure
Phase stability

ABSTRACT

Two commercial 7–8 wt.% Yttria Stabilised Zirconia (YSZ) suspensions were sprayed by Suspension High Velocity Oxy Fuel (SHVOF) thermal spraying for advanced high temperature coatings. Heat treatments of the free-standing coatings were conducted at 800 °C and 1000 °C for 72 h. The SHVOF coatings using two liquid carriers: water and ethanol, behaved differently in terms of micro-structure and phase stability. The ethanol coatings retained a fully tetragonal composition after heat treatments; while the aqueous coatings, however, underwent the undesirable tetragonal to monoclinic phase transformation at 1000 °C, which is lower than previously reported temperatures (> 1200 °C) in thermal sprayed YSZ coatings. The heat treatments not only resulted in densification of both coatings, but also caused excessive crystallite growth in aqueous coatings promoting the undesirable phase transformation. On the contrary, the ethanol suspension improved the phase stability by favouring the homogenization of yttrium during spraying.

1. Introduction

High-velocity oxy-fuel (HVOF) is a well-established thermal spraying technique that has been widely used for various engineering applications at high temperatures [1,2]. Molten or semi-molten particles are sprayed onto the surface of the components by means of a supersonic combustion gas stream, producing a well-bonded and dense coating. Modified HVOF thermal spraying using suspensions has been rapidly developed since 1990s when synthesis technologies of nano-materials became available [3]. Suspension enables the use of sub-micron and nano-powders as a feedstock to form unique nano-structured coatings with significant improvement in density, strength and durability over conventional thermal sprayed coatings [4,5]. In particular, suspensions of oxide ceramics such as alumina [6–8], zirconia [9–11] and titania [12–14] have been widely sprayed by both plasma and HVOF techniques designated for wear-resistant coatings, solid oxide fuel cell (SOFC), thermal barrier coatings (TBC), and photo-catalytic applications, etc. Unlike conventional powder-based spraying processes, the preparation of suspensions is crucial for the coatings properties, which involves de-agglomeration and stabilization of the solid particles in an aqueous or organic solvent. The chosen type of solvent strongly influences many aspects in the spraying process, namely droplet size distribution, heat flux to substrate, the particle in-flight behaviour and overall thermal level, coating porosity and hardness, etc. [3]. Water is generally used as the medium for suspension that can effectively disperse fine powders with a typical solid content 10-40 wt.% or even higher. However, on the other hand, the particle heating becomes less efficient due to the consumption of heat from the flame by water vaporization (It requires 2.63 MJ/kg for water compared to 1.01 MJ/kg for ethanol [15,16]). In case of high melting point oxides like zirconia (2715 °C), a higher flame temperature is indispensable, thus the use of organic solvent is more favourable owing to the extra heat generated by the combustion of organic solvent as fuel (the mass enthalpy generated by ethanol is 29.75 MJ/kg [3]).

Recent studies have looked into the behaviours of nano-structured yttria-stabilized zirconia (YSZ) coatings which exhibit superior performance in terms of phase stability and mechanical properties over conventional YSZ coatings [17–19]. Ideally, YSZ containing 7–8 wt% Y_2O_3 (hereinafter referred to as 8YSZ) is required to retain its as-deposited single-phase tetragonal (*t*) structure, designated as *t'*-phase, through the whole coating lifetime [20]. The ZrO_2–$YO_{1.5}$ phase diagram [21] (See Fig. 1) indicates that the *t'*-YSZ is in fact metastable, because the *t'* phase is supersaturated at all temperatures of interest [22]. It is driven to decompose into a mixture of Y-lean (*t*) and Y-rich cubic (*c*) phases [23]. The depleted *t*-phase would then be susceptible to transform to monoclinic (*m*) phase on cooling after sufficiently extensive

* Corresponding author.
E-mail address: tanvir.hussain@nottingham.ac.uk (T. Hussain).

http://dx.doi.org/10.1016/j.jeurceramsoc.2017.10.026
Received 14 February 2017; Received in revised form 12 October 2017; Accepted 14 October 2017

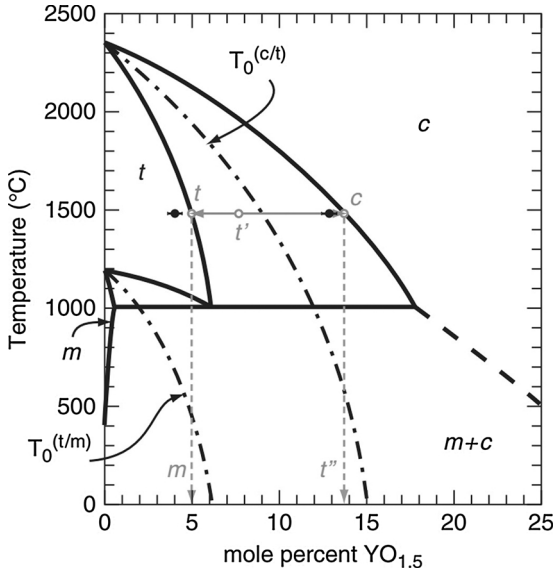

Fig. 1. Zirconia-rich portion of the ZrO_2-$YO_{1.5}$ phase diagram [21].

aging [22]. This deleterious *t* to *m* transformation would induce significant volume change (3–5 vol.%) and subsequently lead to cracks and spallation [24]. With increasing surface temperatures in future turbines, the loss of *t'*-YSZ stability thus becomes more and more critical [25]. A wide range of analytical techniques have been employed to study the microstructural evolution and phase stability of 8YSZ deposited by electron beam physical vapour deposition (EBPVD) and air-plasma spray (APS) [26–29]. Suspension sprayed YSZ coatings, however, are different from EBPVD and APS coatings, in terms of microstructure, porosity, crystallite size, etc., and also behave differently at high temperatures [5].

In this study, we continued the investigations on the suspension sprayed nano-structured YSZ coatings by studying the effect of suspension medium on the microstructure and phase stability of coatings. The aim is to provide a better understanding of the relationships between suspension properties and the performance of SHVOF sprayed YSZ coatings for high temperature applications. Two solvents: water and ethanol, were used as suspension media to produce coatings with vastly different properties. Possible mechanisms were also discussed by analysing the lattice parameter, phase composition, crystallite size and micro-strain of coatings.

2. Experimental procedure

2.1. Materials

Two commercially available suspensions (Innovnano, Coimbra, Portugal) containing ZrO_2–4 mol% (7–8 wt.%) Y_2O_3 (YSZ) were used: an aqueous suspension (hereafter referred to as A-YSZ), and an ethanol suspension (hereafter referred to as E-YSZ). According to the supplier's information, both suspensions were prepared from the same sub-micron-powders, which had the particle size distribution (D_{50} = 0.47 μm) and equal weight of YSZ per weight of suspension ratio of 25%. The suspension was sprayed onto AISI 304 stainless steel substrates of dimensions 60 × 25 × 2 mm^3 with a nominal composition of Fe-19.0Cr-9.3Ni-0.05C (in wt.%). stainless steel. Free standing coatings were achieved by spraying the coating onto aluminium substrates followed by dissolving the aluminium substrates in Sodium Hydroxide leaving behind only the YSZ coating. The use of free-standing coatings could negate the coating-substrate interaction during heat treatments (including heating and cooling) that may induce deformation, residual stress and spallation.

2.2. Spray processes

A modified UTP/Miller Thermal HVOF system (Appleton, WI, USA) with a direct injection at the centre of the gas mixing block was used to spray the suspension. A schematic drawing of the SHVOF system is shown in Fig. 2, and the spraying parameters are listed in Table 1. The SHVOF setup has a modified mixing block and a modified gun back body without any modification to the combustion chamber and the nozzle. The suspension injector had a diameter of 0.3 mm to inject the suspension into the centre of the combustion chamber. A 22 mm long combustion chamber with 110 mm long barrel nozzle was used in this study. The suspension was fed using a pressurised 2 L vessel equipped with a mechanical stirrer. Both suspensions were homogenised for 45 min prior to spraying using a mechanical stirring system to ensure uniform dispersion of the YSZ sub-micron particles in solution and consistent flow onto the substrate without clogging of the nozzle. The pressure of the feeding system was fixed at 6 bar during the spray. Prior to spraying, the substrate were grit-blasted using F100 brown alumina with size range from 0.125 to 0.149 mm, cleaned in an ultrasonic bath to remove any embedded alumina particles and finally, cleaned in acetone. The substrates were then mounted onto a carousel rotating at 73 rpm with a vertical axis of rotation. The rotation speed was set to impart a surface velocity to the substrates of approximately 1 m/s across the spray path. The SHVOF gun was mounted on a z-axis traverse unit in front of the rotating carousel and it was set to a stand-off distance from the surface of the substrate of 85 mm. The gun was scanned

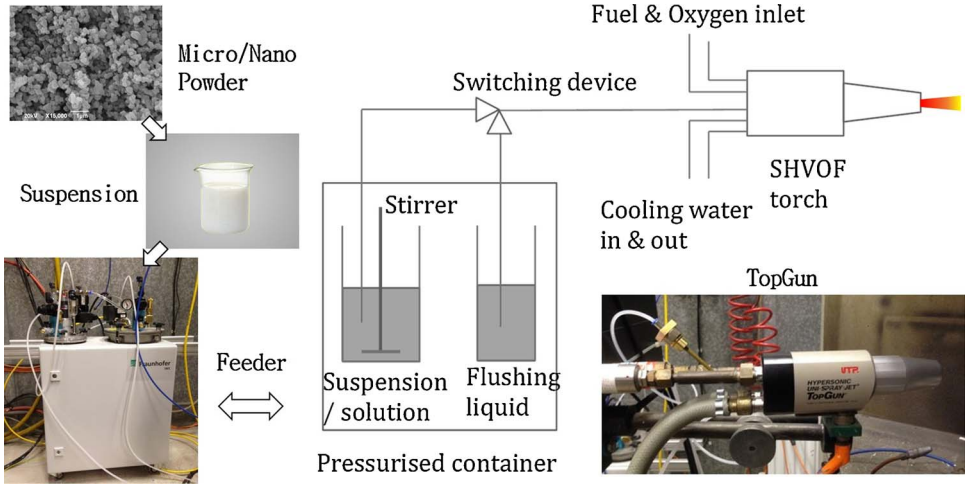

Fig. 2. Schematic drawings and photos showing the experimental setup for SHVOF.

Table 1
Spraying parameters for SHVOF of YSZ suspensions.

Parameter	Value
Gun stand-off distance (mm)	85
Feed pressure (bar)	6
Substrate rotation (rpm)	73
Gun vertical velocity (mm/s)	5
Hydrogen flow (slpm)	624
Oxygen flow (slpm)	312

slpm = standard litre per minute.

vertically up and down at 5 mm/s to build up a coating of the required thickness. The flow rates were set using a volume control system for fuel gas (hydrogen) and oxygen. Hydrogen was used as a combustion fuel which results in the cleanest combustion products and the chance of carbon contamination in the coating is significantly reduced [12]. Both coatings were obtained after 40 passes. During and after the spray run, compressed air jets were directed towards the substrates to provide cooling. At the end of each spray run de-ionised water was supplied to clean the nozzle.

2.3. Heat treatment

Heat treatments of the free-standing coating were conducted using a Carbolite furnace (Bemaford, Sheffield, England) at temperatures of 800 °C and 1000 °C for 72 h in air. Although in previous studies on the phase evolution of APS *t'*-YSZ, the as-sprayed coatings were treated at relatively higher temperatures: 982–1482 °C [22,26]. Lower temperatures were chosen because, for SHVOF coatings, nano-particles have higher surface area/volume ratio and therefore can be easily sintered and densified [30]. Upon completion of the heat treatment the samples were allowed to furnace cooling to prevent unnecessary stresses and thus preserving the coating's structural integrity.

2.4. Characterization

The samples were sectioned transversely with a SiC slitting wheel in a precision cutting saw, then mounted in conductive resin, grounded, polished down to 1 μm surface finish, and finally carbon coated prior to SEM investigations. The cross-sectional microstructure of the polished coatings were analysed using a Phillips XL30 (Eindhoven, The Netherlands) SEM in backscattered electron mode (BSE). The morphology of the YSZ feedstock was analysed using secondary electron (SE) imaging in the same SEM equipment, having dried the aqueous suspension in a furnace at 150 °C for 4 h to obtain dried YSZ powder. Quantitative analysis of the vertical micro-cracks in the A-YSZ and E-YSZ as-sprayed coatings was based on the cross-sectional SEM images with a coatings length of 1 mm. Mercury Intrusion Porosimetry (MIP) Micrometric AutoPore IV 9500 (Texas, USA) was employed to study the porosity of the two as-sprayed free-standing coatings, in which mercury is forced into the sample pores under pressure from 0.53 to 60,000 psia. This method has generally been used to characterise the interconnected porosity over a size range of micrometers to nanometers, which was reported in our previous work [31] and others [32,33]. Results are presented in the form of intrusion volume of mercury per gram vs. pressure where pore diameter (d) is calculated from the pressure values using Washburn's equation

$$d = \frac{-4\sigma \cos\theta}{P} \quad (1)$$

Where σ is surface tension of mercury, and θ is the contact angle between mercury and the pore wall, and these values were assumed to be 0.485 N m^{-1} and 130°, respectively. Free standing deposits of dimension 10 × 8 × 1 mm were used for the mercury intrusion tests. Total mercury intrusion (mL/g) values were converted to volume percentages of porosity of the deposits assuming that the density of both A-YSZ and E-YSZ is 6.05 g/cm^3. It is worth noting MIP can only be used to measure the open porosity which is connected to the surface of the coatings. In this case, the surface morphology of the coatings could largely affect the pore size distribution and therefore, any pores larger than 1 μm are not considered in this measurement. The porosity was also analysed by Image Pro-Plus (6.0, Media Cybernetics, Rockville, USA) software with Pseudo-Colour function to highlight features of interests with same threshold on SEM images. Micro-hardness was measured on the polished coatings cross-section using a Buehler 1600 Series Micro-hardness Tester (Illinois Tool Works, USA) by a Vickers indenter at a load of 10gf. The chosen load was small enough to avoid any cracks during indentation, and also large enough to create clear indentation on the coating cross-section [34]. Surface roughness of the as-sprayed coatings were measured by stylus surface profilometry (Talysurf CLI 1000 Profilometer, Leicester, U.K.) with a resolution of 40 nm. Phase composition of each sample was achieved by XRD analysis using a Siemens D500 (Germany) with Cu$K\alpha$ produced at 40 kV and 25 mA. The 2θ diffraction angle range was from 10° to 90° with step width of 0.05° and time per step of 2 s. Rietveld refinement (TOPAS V5 software package) was used to determine the $c/a\sqrt{2}$ parameter, where c and a are the unit cell dimensions. Rietveld refinement is an analysis technique for the calculation of lattice parameters [35–37]. Quantitative Rietveld refinement was employed to determine the quantity of each phase (*t*- and *m*-phase), and principles of whole powder pattern modelling (WPPM) were used for crystallite size and micro-strain calculations [36].

3. Results

3.1. Microstructure

In Fig. 3, feedstock YSZ particles dried from the aqueous suspensions were observed in secondary electron (SE) mode in SEM showing the size of individual particle. YSZ particles from suspensions form agglomerates due to drying and the typical particle diameters were in the order of 400–500 nm, which agrees with the measurement of the

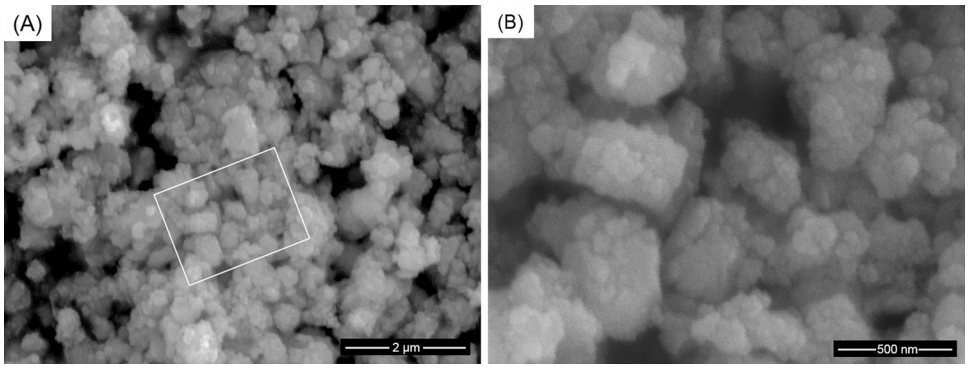

Fig. 3. Feedstock YSZ particles as observed in secondary electron (SE) mode in SEM showing particle agglomeration and the size of individual crystallites (A) low and (B) high magnification.

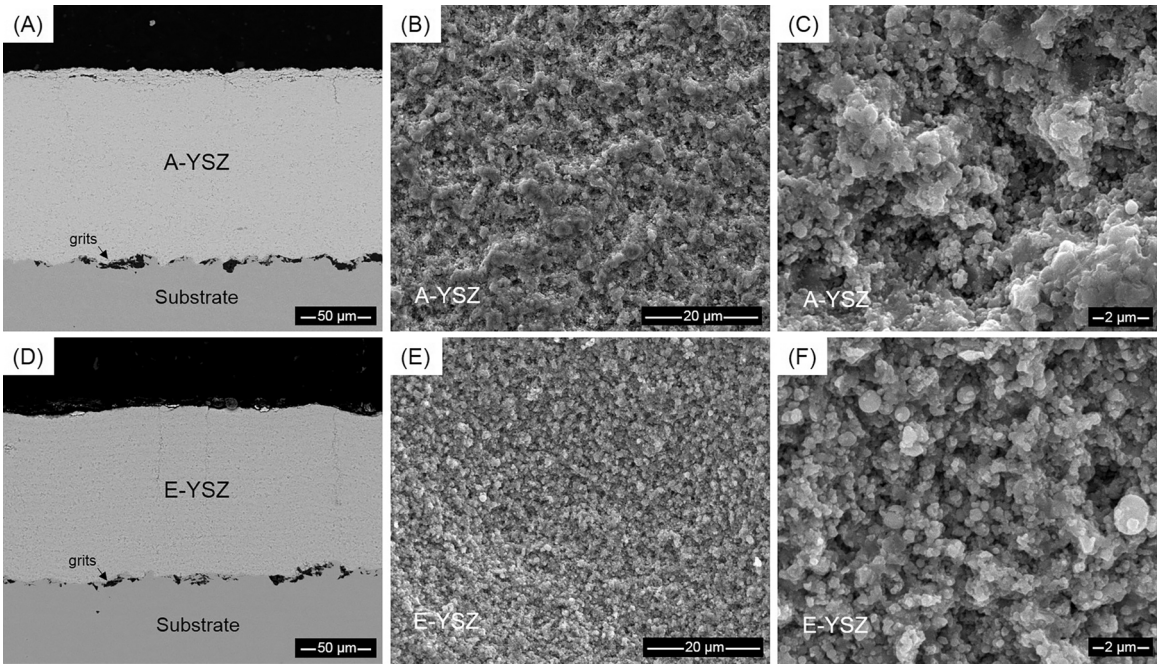

Fig. 4. SEM images showing the cross-sectional microstructure and surface morphology of as-sprayed SHVOF coatings: (A–C) A-YSZ (Aqueous) and (D–F) E-YSZ (Ethanol).

particle size distribution (D50 = 0.47 μm) as provided by the supplier. The crystallite size determined from XRD patterns (discussed in section 4.2) is, however, much lower (~20 nm). It indicates that each YSZ particle is consisted of several smaller nano-crystallite, which could even be identified from Fig. 3 (B) under a higher magnification.

Fig. 4 show the cross-sectional microstructure and surface morphology of the as-sprayed SHVOF coatings: (A–C) A-YSZ (Aqueous) and (D ~ F) E-YSZ (Ethanol). Both coatings are dense and thick; while A-YSZ is slightly thicker (130–135 μm) than E-YSZ (110–120 μm) indicating a higher deposition efficiency with aqueous based suspension. The dark contrast features at the coating substrate interface are embedded alumina grit from the grit blasting operation. Vertical cracks are observed in both coatings originating at the surface that propagated part way through the coating thickness. The vertical micro-cracks are more pronounced in the E-YSZ coating cross-section with a crack density of 10 cracks/mm than that of A-YSZ (5 cracks/mm) and the inter-pass porosities are also clearly visible in E-YSZ coating. From the surface morphology in Fig. 4 (B) and (E), the A-YSZ coating is composed of large features and the E-YSZ coating is composed of much finer features. The surface profilometry results show that A-YSZ (R_a = 2.3 ± 0.3 μm) coating has a slightly lower surface roughness than E-YSZ (R_a = 3.9 ± 0.4 μm). In Fig. 4 (C) and (F) under a higher magnification, larger features are observed on A-YSZ; while the E-YSZ has more spherical features with smaller size on the surface. The spherical features are an indication of particle melting and solidification of the smaller droplets in the process.

3.2. Porosity

MIP was used to characterise the open pore size distribution of the as-sprayed A-YSZ and E-YSZ coatings, which is a reliable porosity measurement method for ceramic coatings [38–40]. Fig. 5 plots the incremental and cumulative porosity vs. pore diameter. The E-YSZ has larger pores with the size range of 0.1–1.0 μm and 0.02–0.03 μm; while A-YSZ has finer pores with a size below 0.025 μm. The cumulative porosity of E-YSZ is 10.98 vol.% which is slightly lower than the value from imaging analysis (14.9 ± 1.9%). The cumulative porosity of A-YSZ is only 2.19 vol.%, which is much smaller than the value from imaging analysis (12.6 ± 1.7%). Both the measurement techniques show that A-YSZ has less porosity than that of E-YSZ. It should be noted that MIP is a robust porosity measurement technique for surface connected porosity and it cannot measure closed porosities. On the other hand, image analysis can measure both open and close porosities although it can suffer from issues related to thresholding and resolution limit of the SEM images of sub-micrometre pores. The higher MIP value indicates that the A-YSZ might have more closed pores than E-YSZ. Fig. 6 shows the cross-sectional microstructures and porosity of both coatings before and after heat treatments at 800 °C and 1000 °C for 72 h. The porosities of the coatings along with standard error in means are presented in Fig. 6. The porosity of the as-sprayed E-YSZ is around ~2.5% higher than that of the as-sprayed A-YSZ. After heat treatments, both coating have experienced significant densification with decreased porosity. Particularly in A-YSZ after the 72 h 1000 °C heat treatment as shown in Fig. 6(C), the fine scale pores appear to have coalesced to form micro-sized pores, and the lamellar microstructure has disappeared. Micro-hardness of all the samples before and after heat treatment are listed in Table 2, showing an increase in both coatings after heat treatment. It also identifies the A-YSZ coating as harder than E-YSZ after each heat treatment, as well as in the as-sprayed state. In general, the micro-hardness of sintered YSZ materials largely depends on its porosity or density [41]. Fig. 7 shows the micro-hardness as a function of porosity for sintered YSZ as plotted according to the empirical curve-fit equation [41–43]. The porosities of the SHVOF coatings are estimated according to this equation (See Table 3). The calculated values are slightly higher than the image analysis results but indicating the same trend.

3.3. Phase stability

The XRD analysis as displayed in Fig. 8 identifies the phases present in the dried YSZ suspension powder, and as-sprayed coatings A-YSZ and E-YSZ. The XRD analysis identifies that the tetragonal phase, labelled as '*t*', is present in the YSZ powder along with some presence (14.1 ± 0.3 wt.%; please note that the calculated error is derived from the mathematical algorithm employed, see Madsen et al. [44]) of the monoclinic phase, labelled as '*m*'. The as-sprayed coatings of A-YSZ and E-YSZ were identical in phase composition, both containing solely the tetragonal phase. Fig. 9 shows the combined XRD patterns for both

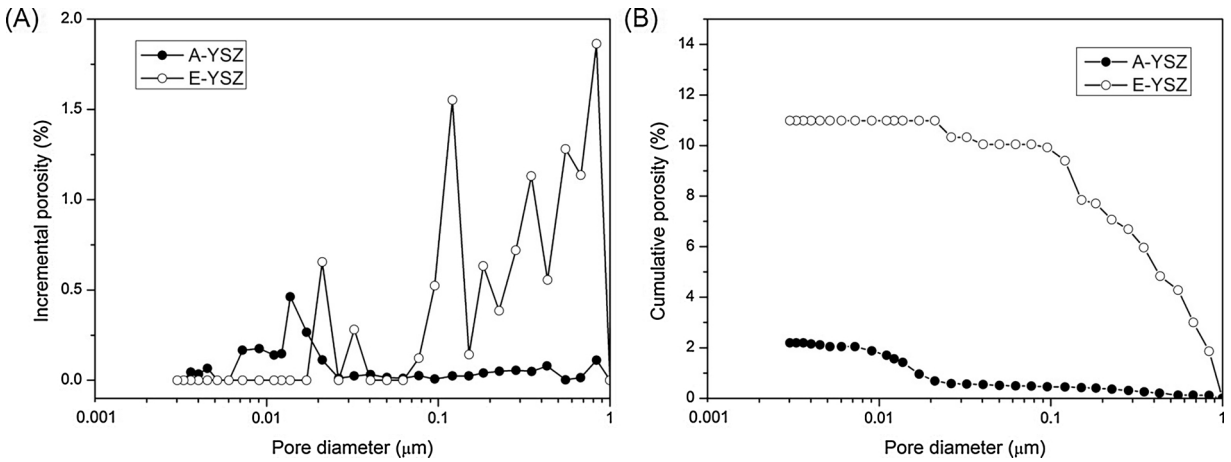

Fig. 5. Mercury intrusion porosimetry (MIP) results: (A) Incremental porosity and (B) cumulative porosity as a dependency of pore size of free-standing as-received A-YSZ and E-YSZ.

coatings after 72 h heat treatments at 800 °C and 1000 °C. The pattern shows that heat treatments of 800 °C and 1000 °C have not affected the phase composition of the E-YSZ coating, neither has the 800 °C heat treatment affected the A-YSZ coating, as they have both retained their entirely tetragonal composition. The 1000 °C 72 h heat treatment of the A-YSZ coating, however, incurred phase transformation. Diffraction peaks of the *m*-phase are identified and the Rietveld Refinement results show that 4.5 ± 0.4 wt.% of the coating transformed to the monoclinic phase. These results show that the A-YSZ and E-YSZ coatings did not behave the same in phase stability when exposed to 1000 °C. This phase transformation in plasma sprayed YSZ was demonstrated earlier by *Miller* et al. [23] during cooling after exposure to temperatures greater than 1200 °C. It was also reported by *Trice* et al. [45] that this transformation did not occur until exposure to 1400 °C. This study shows that the SHVOF coating sprayed from an aqueous suspension can undergo this transformation after an exposure to 1000 °C, which is significantly lower than previously reported temperatures on APS and EBPVD YSZ.

4. Discussion

The above results show that the SHVOF coatings using different suspensions behaved differently in terms of micro-structure and phase stability during heat treatment. In this section, possible mechanisms for the micro-structural and phase evolutions of SHVOF YSZ coating will be discussed by examining the crystal structure, crystallite size, and micro-strain.

Table 2
Micro-hardness of the SHVOF coatings.

	A-YSZ (GPa)	E-YSZ (GPa)
As-sprayed	6.1 ± 0.5	5.6 ± 0.3
800 °C 72 h	9.1 ± 1.0	7.3 ± 1.1
1000 °C 72 h	9.2 ± 0.9	7.5 ± 0.6

4.1. Phase evolution

Previous studies employed XRD to investigate the phase evolution of 7–8 wt.% (3.8–4.4 mol% Y_2O_3) YSZ after aging at high temperatures [46–49]. They have found a linear relationship between the concentration of Y_2O_3 and the lattice parameters $c/a\sqrt{2}$ (also referred to as 'tetragonality') over a large range of concentration of Y_2O_3. *Ilavsky* et al. [50] has determined the cell parameter variations $c/a\sqrt{2}$ as a function of the amount of Y_2O_3 in mol% (x) as the following equation over the

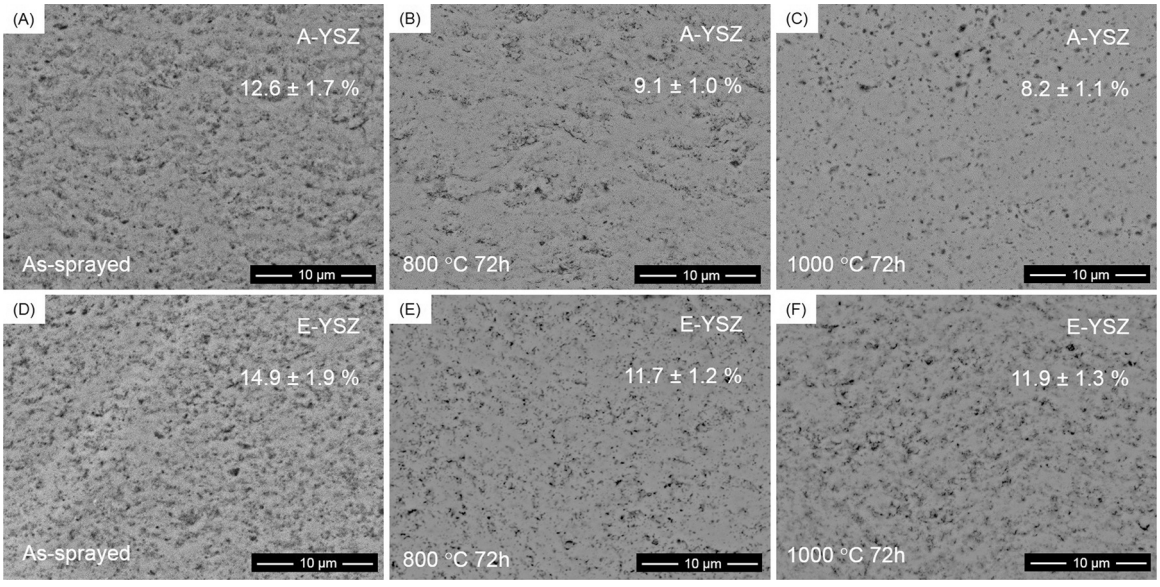

Fig. 6. BSE images showing the cross-sectional microstructure and porosity of (A–C) A-YSZ and (D–E) E-YSZ in as-sprayed state, after treatment at 800 °C and 1000 °C for 72 h, respectively.

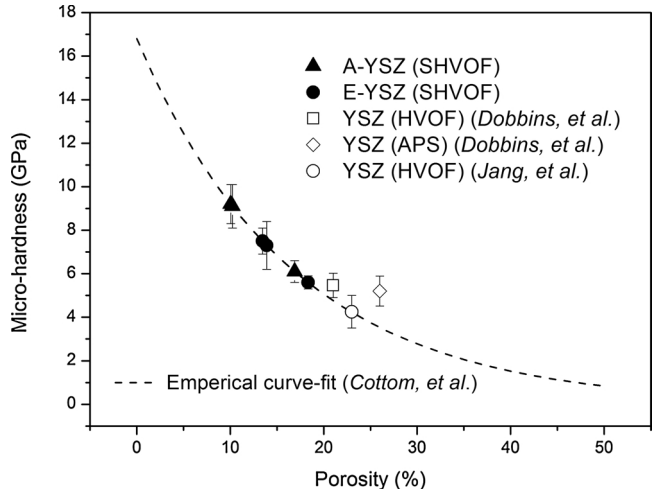

Fig. 7. Micro-hardness as a function of porosity for sintered YSZ as plotted according to the empirical curve-fit through the data, $H = 16.807e^{-0.06P}$ $R^2 = 0.95$, which is representative of the micro-hardness dependence on porosity based on the experimental data from *Cottom* et al. [41]. The micro-hardness of A-YSZ and E-YSZ are marked by solid symbols, while conventional HVOF and APS YSZ coatings from *Dobbins* et al. [42] and *Jang* et al. [43], are marked by open symbols.

Table 3
Calculated porosity of the SHVOF coatings according to the empirical curve-fit equation $H = 16.807e^{-0.06P}$, $R^2 = 0.95$ and image analysis results.

	Calculated		Image analysis	
	A-YSZ (%)	E-YSZ (%)	A-YSZ (%)	E-YSZ (%)
As-sprayed	16.9	18.3	12.6 ± 1.7	14.9 ± 1.9
800 °C 72 h	10.2	13.9	9.1 ± 1.0	11.7 ± 1.2
1000 °C 72 h	10.0	13.4	8.2 ± 1.1	11.9 ± 1.3

concentration of Y_2O_3 up to about 7 mol% (Data was retrieved from the original plot and linear fitted with $R^2 = 1$):

$$c/a\sqrt{2} = 1.02257 - 0.0032x \quad (2)$$

Eq. (2) can be used to estimate the Y_2O_3 composition (mol%) using the tetragonality ($c/a\sqrt{2}$) obtained from the XRD patterns. The results are plotted in Fig. 10 and the detailed data is summarized in Table 4. In Fig. 10(A), it is obvious that the tetragonality of as-sprayed A-YSZ has a distinctive lower value in comparison with those of the YSZ-suspension particles and as-sprayed E-YSZ. The as-sprayed A-YSZ should therefore contain a higher content of Y_2O_3 (4.94 mol%) than the YSZ suspension (4.31 mol%) and as-sprayed E-YSZ (4.35 mol%) as plotted in Fig. 10(B). The increase of the Y_2O_3 content in the as-sprayed A-YSZ can only be caused by the inhomogeneous distribution. This is simply based on the principle of mass conservation as both A-YSZ and E-YSZ coating are both originated from the same the YSZ feedstock. It is also highly unlikely that it will incur any loss of Y_2O_3 during SHVOF spraying by decomposition or evaporation (the boiling point of Y_2O_3 is over 4300 °C). Accordingly, it can be argued that the less homogeneity of Y_2O_3 (i.e., lower tetragonality and predicated overall higher Y_2O_3 mol %) in the as-sprayed A-YSZ could be due to a combination of both Y-rich and Y-lean *t*'-phases, which however cannot be distinguished using XRD. Krogstad et al. [26] confirmed the non-even distribution of Y in APS YSZ coatings after aged for 7.8 h at 1482 °C using a high angle annular dark field (HAADF) scanning transmission electron microscopy (STEM). TEM observation has provided key insight because of the enhanced sensitivity of electron diffraction to the anion lattice over XRD analysis, which is able to separate the Y-rich and Y-lean areas but the average concentrations of Y for both coatings should be equal due to conversation of mass. As mentioned earlier, the Y-lean t'-phase in YSZ is more susceptible to the deleterious transformation on cooling. On the other hand, the as-sprayed E-YSZ has a similar Y_2O_3 content with the YSZ suspension. This is plausible as the ethanol suspension has a higher flame temperatures during spraying leading to more complete melting of YSZ agglomerates and therefore results in more homogeneity of Y_2O_3. In addition, the as-sprayed A-YSZ has a tetragonality value much closer to 1 indicating a higher potential of the existence of a third particular metastable tetragonal phase, called *t*"-phase (See Fig. 11). Conventional XRD is unable to distinguish this *t*" phase from a cubic phase since the cell parameters ratio of this tetragonal phase is equal to the unity. However, it is still considered as a tetragonal phase because of a slight distortion of the anionic network [24]. The potential existence of *t*"-phase in the as-sprayed A-YSZ could also deteriorate the homogeneity of *t*'-phase and therefore contribute to a less stable *t*'-phase than E-YSZ during heat treatment.

4.2. Crystallite size and micro-strain

The phase evolution of 7–8 wt.% YSZ can be rationalized on the basis of a simple diffusion-limited kinetics argument, which assumes that the destabilization of *t*'-YSZ is controlled by a critical diffusion distance of Y^{3+} (toward the incipient cubic phase) [22]. At higher operating temperatures, faster diffusion kinetics would lead to accelerated segregation and crystallite growth, which would significantly promote *t* to *m* transformation [22]. This phenomenon becomes essential for the phase stability of SHVOF YSZ coatings, which is consisted of nano-sized crystallites with a larger tendency to grow during heat treatment. In this study, the crystallite size is determined by the coherent diffracting crystalline domains (CDD) as obtained by WPPM incorporated Rietveld Refinement of the XRD patterns of YSZ free-standing coatings, which is shown in Fig. 12. Significant crystallite growth is observed in A-YSZ after 72 h' heat treatment at 1000 °C increasing from ~55 nm to ~100 nm; while the E-YSZ remains at 50–60 nm. The reason for the excessive crystallite growth in A-YSZ after 72 h treatment at 1000 °C can be explained by the difference in the microstructures of A-YSZ and E-YSZ. As mentioned earlier, as-sprayed A-YSZ is relatively denser with less porosity than E-YSZ, which therefore shortens the densification (sintering) process. It is worth noting that the sintering and grain growth are two competing processes, in which case, during the heat treatment at 800 °C and 1000 °C for 72 h, the densification process in A-YSZ should have completed earlier than E-YSZ which causes excessive crystallite growth in A-YSZ. On the other hand, it is possible that the inhibited grain growth in the E-YSZ is attributed to the higher levels of porosity and larger pore sizes (see MIP results as shown earlier in Fig. 5) trapped in the grain boundaries, which slowed down the grain boundary diffusion and subsequent grain growth.

Suspension droplet size is a key factor in determining the coating properties, as it plays a prominent role in determining the size of the of the molten droplet which in turn directly correlates to the grain sizes in the coatings. However, the atomization of the suspension inside the combustion chamber is a highly complex process. Suspension properties like viscosity and surface tension, as well as geometry and dimensions of the atomization nozzle along with properties of the surrounding fuel gas and oxygen flows all interact in the formation of the droplets and their resulting coating microstructure and the grain size [51]. It is worth mentioning that in SHVOF thermal spraying, particle injection is directly inside the combustion chamber and thus a considerably good heat transfer of the particles can be realised. This enables complete melting and homogenisation of the YSZ nano-crystallite feedstock, which completely removes the impurity *m*-phase. The molten droplet then solidifies with the nucleation of stable *t*-phase upon impact on the substrates. The solidification temperature at which the nucleation takes place depends on the cooling rate [51–53]. SHVOF torches can reach very high gas velocities (> 2000 m/s) [3], and the substrates are typically cooled with compressed air jets, which all contribute to rapid

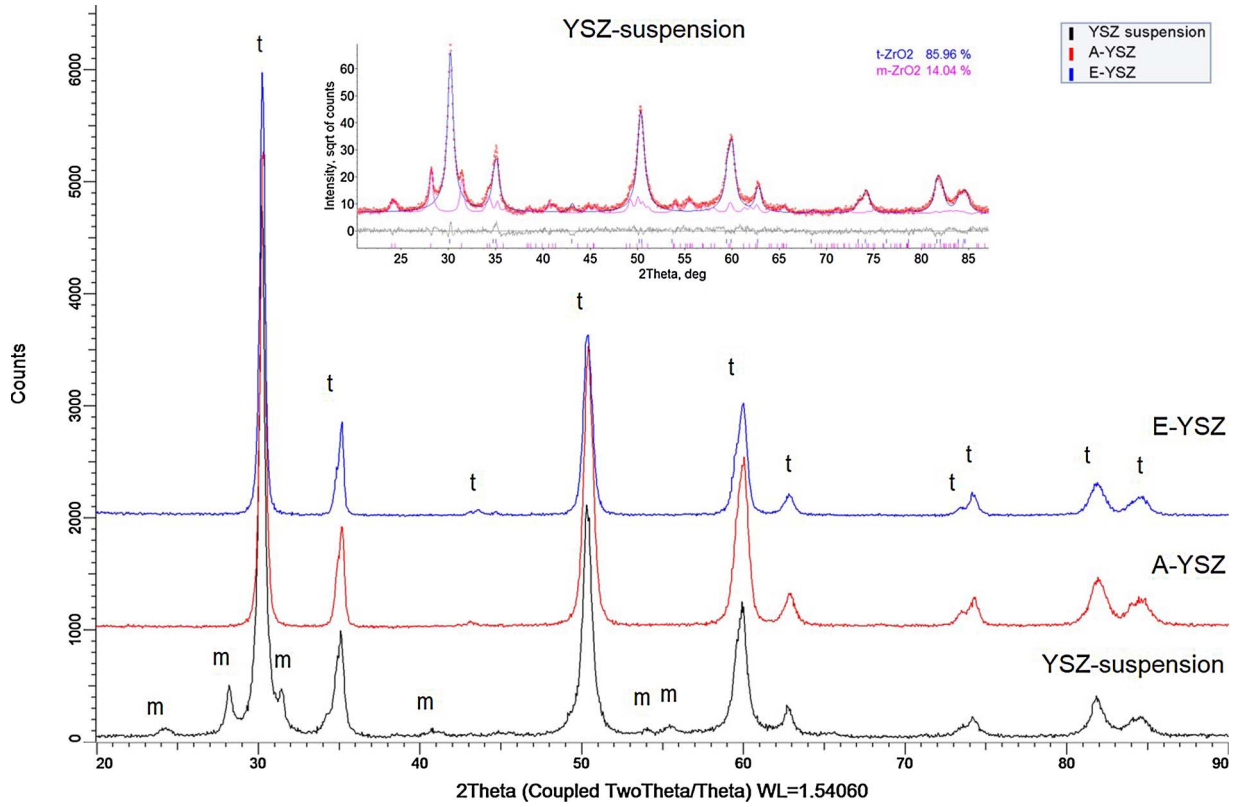

Fig. 8. Combined XRD patterns for the dried YSZ suspensions powders and as-sprayed coatings: A-YSZ and E-YSZ. The inset is the result of Rietveld refinement of dried suspension powder pattern showing tetragonal (t-ZrO_2) and monoclinic (m-ZrO_2) zirconia with corresponding quantities of ~86 and ~14 wt.% (the Rwp factor of the refinement is 11.3).

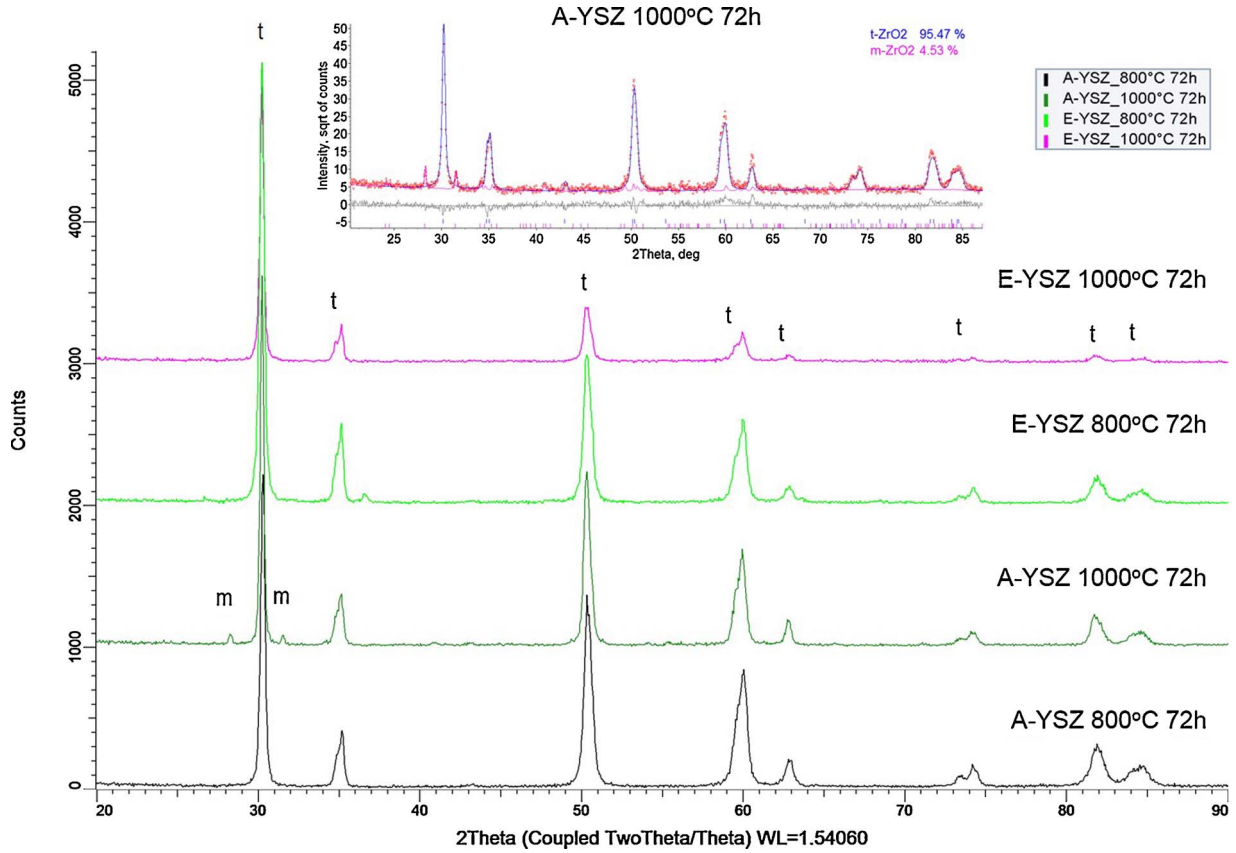

Fig. 9. Combined XRD patterns for A-YSZ and E-YSZ before and after heat treatment. The inset is the result of Rietveld refinement of A-YSZ pattern treated at 1000 °C for 72 h and shows dominant presence of t-ZrO_2 and ~4 wt.% of m-ZrO_2 (the Rwp factor of the refinement is 19.3).

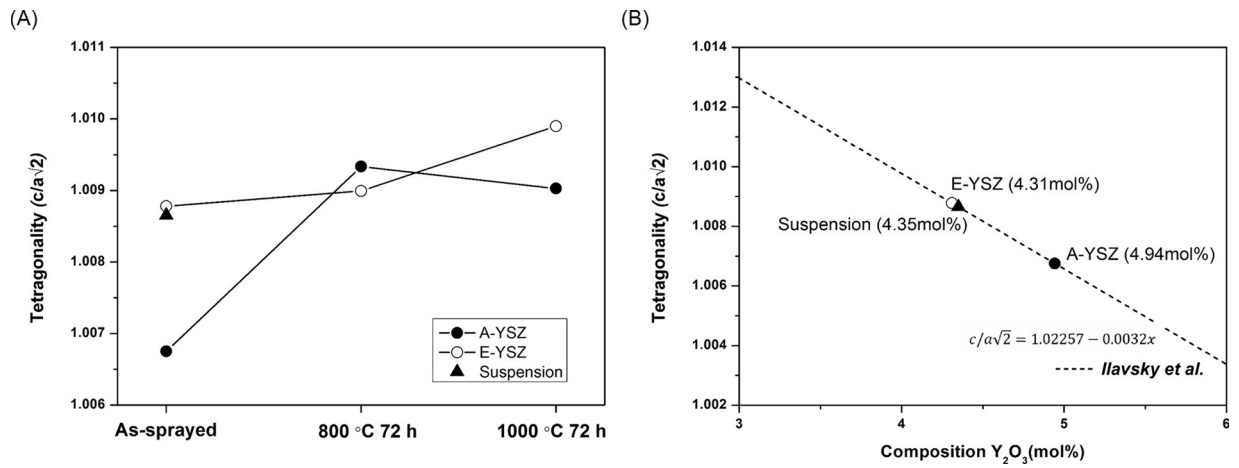

Fig. 10. (A) Plot of the lattice parameter ratio of c/a√2 of YSZ coatings before and after treatment. (B) Effect of the composition of Y_2O_3 on the tetragonality (c/a√2) of as-sprayed A-YSZ and E-YSZ coatings. The dashed line is plotted according to the results from *Ilavsky* et al. [50].

Table 4
Calculated concentration of Y_2O_3 (mol%) in the SHVOF coatings by Eq. (2).

	A-YSZ (mol%)	E-YSZ (mol%)
As-sprayed	4.94	4.31
800 °C 72 h	4.14	4.24
1000 °C 72 h	4.23	3.96
Suspension	4.35	

cooling of the molten droplets. This results in a high nucleation rate as well as a low growth rate of crystallites as inhibited by the short residence time due to rapid acceleration in the flame and rapid cooling upon impact, all of which contribute to the formation of nano-crystallized YSZ coatings. Micro-strains (ε) are also very common in nano-crystalline materials, which is mainly attributed to solid solution inhomogeneity by creating a distribution of *d*-spacing for a crystallographic plane [54]. Fig. 13 shows the micro-strain in YSZ SHVOF coatings as obtained by WPPM approach from the XRD patterns. Both coatings show a decreasing trend after heat treatments. In particular, the as-sprayed A-YSZ possesses a larger micro-strain indicating a higher degree of solid solution inhomogeneity than E-YSZ. This agrees well with the previous discussion that the as-sprayed A-YSZ has lower homogeneity in phase and compositions leading to a less stable *t'*-phase.

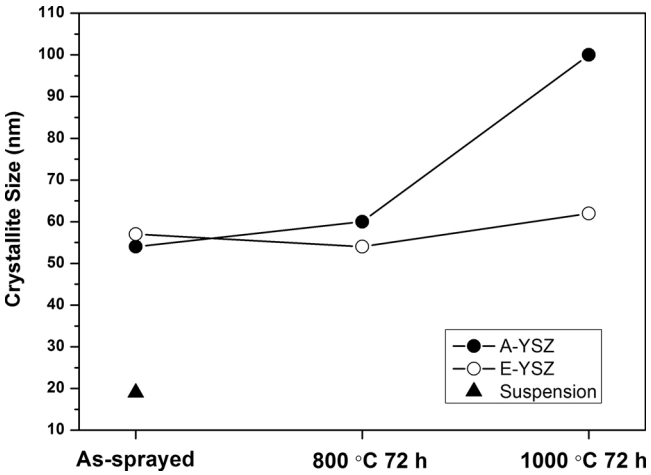

Fig. 12. Plot of the average *t*-ZrO_2 crystallite sizes in YSZ coatings as obtained by WPPM (Whole Powder Pattern Modelling) incorporated Rietveld refinement of the XRD patterns.

4.3. Aqueous and ethanol suspensions

Both suspensions used in this study are commercial products possessing the same solid content and long-term stability, and main physical properties of these two solvents are listed in Table 5. The main difference here concerns with the flame temperatures, as ethanol has a significant mass enthalpy of reaction at 29.75 MJ/kg; while in case of water, particle heating is less efficient as gas temperatures are significantly decreased. In addition, the vaporization of water would consume more heat than ethanol as its mass enthalpy of vaporization is

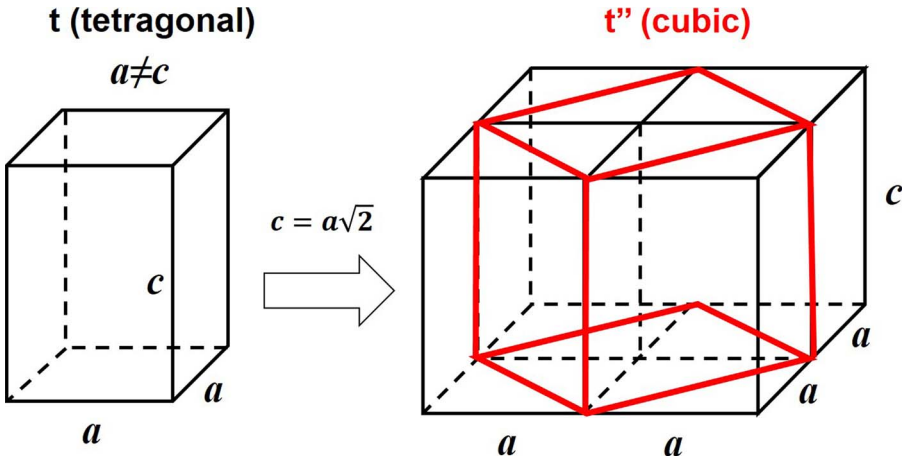

Fig. 11. Schematic drawing of crystal lattice indicating the transformation from *t* to *t*'' phase.

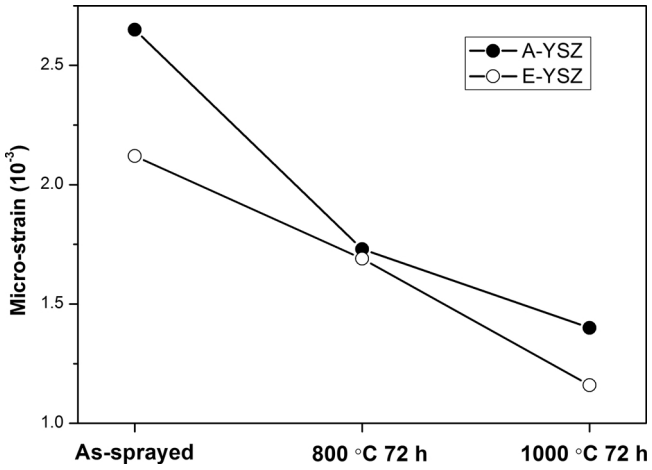

Fig. 13. Plot of the micro-strains in *t*-ZrO_2 phase in YSZ coatings as obtained by WPPM (Whole Powder Pattern Modelling) incorporated Rietveld refinement of the XRD patterns.

Table 5
Physical properties of water and ethanol used for suspension HVOF spraying [3].

	Water	Ethanol
Specific mass, kg/m^3 at 20 °C	998	790
Vaporization temperature, °C	100	78
Mass enthalpy of vaporization, kJ/kg	2260	846
Volume enthalpy of vaporization, kJ/L	2253	657
Mass enthalpy of reaction, kJ/kg	–	29,750
Volume enthalpy of reaction, kJ/L	–	23,367

2.26 MJ/kg, nearly two times high than that of ethanol, which further decreases the flame temperature. On the other hand, however, in case of water, the chamber pressure and consequently gas velocity increased due to the presence of water vapour resulting in a denser microstructure [3]. In general, the type of solvent plays an important role in suspension spraying. Primary atomization basically depends on nozzle geometry, relative velocity of liquid to surrounding gas and gas/liquid properties such as density, viscosity, and liquid surface tension [52]. The behaviour of a liquid during atomization can be described by the dimensionless Weber number *We* and Reynolds number *Re*. Basically, Re number gives the relationship of fluid inertia to viscosity, and We number expresses the ratio of the deforming inertia force of the medium to surface tension of the droplet. In general, high values for both (*Re* and *We*) promote a more rapid and finer atomization. For water (w) and ethanol (e), typical values can be found in the literature, which are in the range of $Re = 1500$ (w), 3300 (e) and $We = 15$ (w), 150 (e) [55]. In this case, the ethanol should have finer atomization and smaller droplets due to higher *Re* and *We* values, therefore resulting in the formation of re-solidified agglomerates and increased porosity level in the coatings; while the water should have larger droplets and denser coatings.

Last but not the least, although the SHVOF YSZ coatings using aqueous suspension has great advantages in microstructure with less porosity and nano-sized crystallites (about 60 nm), it has a disadvantage in terms of phase stability after long-term exposure to elevated temperatures (over 1000 °C) due to an accelerated densification (sintering) rate and significant crystallite growth that would promote the undesired phase transformation. For applications, considering the SOFC industry is striving to operate at temperatures lower than 1000 °C and require electrolytes with very dense microstructures [56], YSZ SHVOF coatings using aqueous suspensions show promise in this area but may be restricted to specific applications (e.g. coating on components with complex shapes exclusively by thermal spraying). On the other hand, the E-YSZ coating, obtained by spraying an ethanol suspension demonstrated relatively higher porosity corresponding to lower thermal conductivity [57], and better phase stability, indicating some potential as an alternative for TBC applications although it might be too dense to achieve sufficiently thermal protection.

5. Conclusions

In this study, we have investigated SHVOF thermal sprayed YSZ coatings with two commercial 7–8 wt.% YSZ suspensions on the coating microstructure and phase stability during heat treatment. The coatings were further exposed to heat treatment at 800 °C and 1000 °C for 72 h and then characterised in XRD with Rietveld refinement for phase changes. Regarding the two types of coatings produced, the following conclusions can be drawn:

- The as-sprayed coatings using aqueous suspensions had denser microstructure with less porosity than the coatings sprayed with ethanol suspensions.
- Both as-sprayed coatings comprised entirely t'-phase but the aqueous YSZ had a less stable t'-phase and a more rapid crystallite growth at 1000°C, which led to the phase transformation to the undesirable monoclinic phase after 72h treatment.
- Ethanol suspension stabilized t'-phase by favouring the homogenization of yttrium during spraying, and also inhibiting the crystallites growth during heat treatment.

Acknowledgements

This work was supported by the Engineering and Physical Sciences Research Council [grant number EP/M01536X/1]. The authors would like to thank Dr. Chun Li from the University of Manchester for the helpful discussion on crystallography and Mr. Rory Screaton for the experimental assistance.

References

[1] A. Feuerstein, J. Knapp, T. Taylor, A. Ashary, A. Bolcavage, N. Hitchman, Technical andeconomical aspects of current thermal barrier coating systems for gas turbine engines by thermal spray and EBPVD: a review, J. Therm. Spray Technol. 17 (2008) 199–213.
[2] T. Sidhu, R. Agrawal, S. Prakash, Hot corrosion of some superalloys and role of high-velocity oxy-fuel spray coatings—a review, Surf. Coat. Technol. 198 (2005) 441–446.
[3] A. Killinger, P. Müller, R. Gadow, What do we know, what are the current limitations of suspension HVOF spraying, J. Therm. Spray Technol. 24 (2015) 1130–1142.
[4] F.-L. Toma, L.-M. Berger, C.C. Stahr, T. Naumann, Langner S. Microstructures, Functional properties of suspension-Sprayed Al2O3 and TiO2 coatings: an overview, J. Therm. Spray Technol. 19 (2010) 262–274.
[5] A. Killinger, R. Gadow, G. Mauer, A. Guignard, R. Vaßen, D. Stöver, Review of new developments in suspension and solution precursor thermal spray processes, J. Therm. Spray Technol. 20 (2011) 677–695.
[6] J.W. Murray, A.S.M. Ang, Z. Pala, E.C. Shaw, T. Hussain, Suspension high velocity oxy-fuel (SHVOF)-sprayed alumina coatings: microstructure, nanoindentation and wear, J. Therm. Spray Technol. (2016) 1–11.
[7] F.-L. Toma, L.-M. Berger, S. Scheitz, S. Langner, C. Rödel, A. Potthoff, et al., Comparison of the microstructural characteristics and electrical properties of thermally sprayed Al2O3 coatings from aqueous suspensions and feedstock powders, J. Therm. Spray Technol. 21 (2012) 480–488.
[8] F.-L. Toma, L.-M. Berger, C.C. Stahr, T. Naumann, S. Langner, Thermally sprayed Al2O3 coatings having a high content of corundum without any property-reducing additives, and method for the production thereof. Google Patents 2012.
[9] A. Ganvir, N. Curry, N. Markocsan, P. Nylén, F.-L. Toma, Comparative study of suspension plasma sprayed and suspension high velocity oxy -fuel sprayed YSZ thermal barrier coatings, Surf. Coat. Technol. 268 (2015) 70–76.
[10] A. Killinger, M. Kuhn, R. Gadow, High-velocity suspension flame spraying (HVSFS), a new approach for spraying nanoparticles with hypersonic speed, Surf. Coat. Technol. 201 (2006) 1922–1929.
[11] J. Oberste Berghaus, J.G. Legoux, C. Moreau, R. Hui, C. Deces-Petit, W. Qu, et al., Suspension HVOF spraying of reduced temperature solid oxide fuel cell electrolytes, J. Therm. Spray Technol. 17 (2008) 700–707.
[12] Z. Pala, E. Shaw, J. Murray, N. Senin, T. Hussain, Suspension high velocity oxy-fuel spraying of TiO 2: a quantitative approach to phase composition, J. Eur. Ceram. Soc. 37 (2017) 801–810.
[13] G. Bolelli, V. Cannillo, R. Gadow, A. Killinger, L. Lusvarghi, J. Rauch, Properties of high velocity suspension flame sprayed (HVSFS) TiO2 coatings, Surf. Coat. Technol.

203 (2009) 1722–1732.
[14] F.L. Toma, L.M. Berger, D. Jacquet, D. Wicky, I. Villaluenga, Y.R. de Miguel, et al., Comparative study on the photocatalytic behaviour of titanium oxide thermal sprayed coatings from powders and suspensions, Surf. Coat. Technol. 203 (2009) 2150–2156.
[15] F.L. Toma, A. Potthoff, L.M. Berger, Leyens C. Demands, Potentials, and economic aspects of thermal spraying with suspensions: a critical review, J. Therm. Spray Technol. 24 (2015) 1143–1152.
[16] P. Fauchais, R. Etchart-Salas, V. Rat, J.-F. Coudert, N. Caron, K. Wittmann-Ténèze, Parameters controlling liquid plasma spraying: solutions, sols, or suspensions, J. Therm. Spray Technol. 17 (2008) 31–59.
[17] R.S. Lima, B.R. Marple, Nanostructured YSZ thermal barrier coatings engineered to counteract sintering effects, Mater. Sci. Eng. A 485 (2008) 182–193.
[18] R. Ghasemi, R. Shoja-Razavi, R. Mozafarinia, H. Jamali, Comparison of microstructure and mechanical properties of plasma-sprayed nanostructured and conventional yttria stabilized zirconia thermal barrier coatings, Ceram. Int. 39 (2013) 8805–8813.
[19] A. Keyvani, M. Saremi, M.H. Sohi, An investigation on oxidation, hot corrosion and mechanical properties of plasma-sprayed conventional and nanostructured YSZ coatings, Surf. Coat. Technol. 206 (2011) 208–216.
[20] J.A. Krogstad, M. Lepple, Y. Gao, D.M. Lipkin, C.G. Levi, Effect of yttria content on the zirconia unit cell parameters, J. Am. Ceram. Soc. 94 (2011) 4548–4555.
[21] O. Fabrichnaya, C. Wang, M. Zinkevich, C.G. Levi, F. Aldinger, Phase equilibria and thermodynamic properties of the ZrO2-GdO1.5-YO1.5 system, J. Phase Equilib. Diff. 26 (2005) 591–604.
[22] D.M. Lipkin, J.A. Krogstad, Y. Gao, C.A. Johnson, W.A. Nelson, C.G. Levi, Phase evolution upon aging of air-plasma sprayed t'-zirconia coatings: isynchrotron X-ray diffraction, J. Am. Ceram. Soc. 96 (2013) 290–298.
[23] R.A. Miller, J.L. Smialek, R.G. Garlick, Phase stability in plasma-sprayed, partially stabilized zirconia-yttria, Adv. Ceram. (1981) 241–253.
[24] C. Viazzi, J.-P. Bonino, F. Ansart, A. Barnabé, Structural study of metastable tetragonal YSZ powders produced via a sol–gel route, J. Alloys Compd. 452 (2008) 377–383.
[25] J.A. Krogstad, S. Kramer, D.M. Lipkin, C.A. Johnson, D.R.G. Mitchell, J.M. Cairney, et al., Phase stability of t '-zirconia-based thermal barrier coatings: mechanistic insights, J. Am. Ceram. Soc. 94 (2011) S168–S177.
[26] J.A. Krogstad, R.M. Leckie, S. Kramer, J.M. Cairney, D.M. Lipkin, C.A. Johnson, et al., Phase evolution upon aging of air plasma sprayed t'-zirconia coatings: II-microstructure evolution, J. Am. Ceram. Soc. 96 (2013) 299–307.
[27] V. Lughi, D.R. Clarke, Low-temperature transformation kinetics of electron-beam deposited 5 wt.% yttria-stabilized zirconia, Acta Mater. 55 (2007) 2049–2055.
[28] V. Lughi, D.R. Clarke, Transformation of electron-ream physical vapor-deposited 8 wt% yttria-stabilized zirconia thermal barrier coatings, J. Am. Ceram. Soc. 88 (2005) 2552–2558.
[29] J. Chevalier, L. Gremillard, A.V. Virkar, D.R. Clarke, The tetragonal-monoclinic transformation in zirconia: lessons learned and future trends, J. Am. Ceram. Soc. 92 (2009) 1901–1920.
[30] M. Bai, F. Guo, P. Xiao, Fabrication of thick YSZ thermal barrier coatings using electrophoretic deposition, Ceram. Int. 40 (2014) 16611–16616.
[31] T. Hussain, D. McCartney, P. Shipway, T. Marrocco, Corrosion behavior of cold sprayed titanium coatings and free standing deposits, J. Therm. Spray Technol. 20 (2011) 260–274.
[32] D.K. Panesar, J. Francis, Influence of limestone and slag on the pore structure of cement paste based on mercury intrusion porosimetry and water vapour sorption measurements, Constr. Build. Mater. 52 (2014) 52–58.
[33] G.N. Okolo, R.C. Everson, H.W. Neomagus, M.J. Roberts, R. Sakurovs, Comparing the porosity and surface areas of coal as measured by gas adsorption, mercury intrusion and SAXS techniques, Fuel 141 (2015) 293–304.
[34] G. Strnad, L. Jakab-Farkas, Improving the accuracy of low-load vickers microhardness testing of hard thin films, Procedia Technol. 12 (2014) 289–294.
[35] L. McCusker, Von dreele R, cox D, louer D, scardi P. rietveld refinement guidelines, J. Appl. Crystallogr. 32 (1999) 36–50.
[36] P. Scardi, M. Leoni, Whole powder pattern modelling, Acta Crystallogr. Sect. A Found. Crystallogr. 58 (2002) 190–200.
[37] H.M. Rietveld, The rietveld method, Phys. Scr. 89 (2014) 098002.
[38] R. Vaßen, H. Kaßner, A. Stuke, F. Hauler, D. Hathiramani, D. Stöver, Advanced thermal spray technologies for applications in energy systems, Surf. Coat. Technol. 202 (2008) 4432–4437.
[39] L. Pawlowski, Methods of Coatings' Characterization. The Science and Engineering of Thermal Spray Coatings, John Wiley & Sons, Ltd., 2008, pp. 291–381.
[40] O.J. Whittemore, Mercury porosimetry of ceramics, Powder Technol. 29 (1981) 167–175.
[41] B.A. Cottom, M.J. Mayo, Fracture toughness of nanocrystalline ZrO2-3mol% Y2O3 determined by vickers indentation, Scr. Mater. 34 (1996) 809–814.
[42] T.A. Dobbins, R. Knight, M.J. Mayo, HVOF thermal spray deposited Y2O3-stabilized ZrO2 coatings for thermal barrier applications, J. Therm. Spray Technol. 12 (2003) 214–225.
[43] H.-J. Jang, D.-H. Park, Y.-G. Jung, J.-C. Jang, S.-C. Choi, U. Paik, Mechanical characterization and thermal behavior of HVOF-sprayed bond coat in thermal barrier coatings (TBCs), Surf. Coat. Technol. 200 (2006) 4355–4362.
[44] I.C. Madsen, N.V. Scarlett, L.M. Cranswick, T. Lwin, Outcomes of the International Union of crystallography commission on powder diffraction round robin on quantitative phase analysis: samples 1a to 1 h, J. Appl. Crystallogr. 34 (2001) 409–426.
[45] R. Trice, Y.J. Su, J. Mawdsley, K. Faber, A. De Arellano-Lopez, H. Wang, et al., Effect of heat treatment on phase stability, microstructure, and thermal conductivity of plasma-sprayed YSZ, J. Mater. Sci. 37 (2002) 2359–2365.
[46] H. Scott, Phase relationships in the zirconia-yttria system, J. Mater. Sci. 10 (1975) 1527–1535.
[47] H. Toraya, Effect of YO1. 5 dopant on Unit-Cell parameters of ZrO2 at low contents of YO1. 5, J. Am. Ceram. Soc. 72 (1989) 662–664.
[48] J. Brandon, R. Taylor, Phase stability of zirconia-based thermal barrier coatings part I. zirconia-yttria alloys, Surf. Coat. Technol. 46 (1991) 75–90.
[49] M. Yoshimura, M. Yashima, T. Noma, S. Sōmiya, Formation of diffusionlessly transformed tetragonal phases by rapid quenching of melts in ZrO2-RO1. 5 systems (Rō = ōrare earths), J. Mater. Sci. 25 (1990) 2011–2016.
[50] J. Ilavsky, J.K. Stalick, Phase composition and its changes during annealing of plasma-sprayed YSZ, Surf. Coat. Tech. 127 (2000) 120–129.
[51] L. Pawlowski, Suspension and solution thermal spray coatings, Surf. Coat. Technol. 203 (2009) 2807–2829.
[52] L. Pawlowski, Finely grained nanometric and submicrometric coatings by thermal spraying: a review, Surf. Coat. Technol. 202 (2008) 4318–4328.
[53] R. Jaworski, L. Pawlowski, F. Roudet, S. Kozerski, A.L. Maguer, Influence of suspension plasma spraying process parameters on TiO2 coatings microstructure, J. Therm. Spray Technol. 17 (2008) 73–81.
[54] S.A. Speakman, Estimating Crystallite Size Using XRD, MIT Center for Materials Science and Engineering, 2014.
[55] Z. Dai, G. Faeth, Temporal properties of secondary drop breakup in the multimode breakup regime, Int. J. Multiphase Flow 27 (2001) 217–236.
[56] S.P.S. Badwal, K. Foger, Solid oxide electrolyte fuel cell review, Ceram. Int. 22 (1996) 257–265.
[57] A.G. Evans, D.R. Clarke, C.G. Levi, The influence of oxides on the performance of advanced gas turbines, J. Eur. Ceram. Soc. 28 (2008) 1405–1419.